Journal of Materials Chemistry A

ROYAL SOCIETY OF CHEMISTRY

PAPER

View Article Online
View Journal



Cite this: DOI: 10.1039/d2ta01188c

# Vacancy-engineered $CeO_2$/Co heterostructure anchored on the nitrogen-doped porous carbon nanosheet arrays vertically grown on carbon cloth as an integrated cathode for the oxygen reduction reaction of rechargeable Zn–air battery†

Shuxin Li,[ab] Han Zhang, *[ab] Lin Wu,[ab] Hongwei Zhao,[ab] Lixiang Li,*[ab] Chengguo Sun[ab] and Baigang An *[ab]

A rechargeable zinc–air battery (ZAB) is regarded as a promising energy storage device owing to its high energy density, good safety, and environmental friendliness. However, the development of non-precious metal catalysts for improving the sluggish oxygen reaction kinetics of the air cathode of ZAB still presents a challenge. Herein, nitrogen-doped porous carbon nanosheet arrays vertically grown on carbon cloth decorated with $CeO_2$/Co heterostructure (Co/$CeO_2$–NCNA@CC) as an integrated cathode have been successfully constructed using a facile carbonization–hydrolysis procedure using a metal–organic framework (MOF) as a precursor. The size of $CeO_2$ nanoparticles can be controlled with an average diameter of about 6.0 nm through unique hydrolysis to form the heterostructure with Co species, which are uniformly dispersed on the surface of nitrogen-doped porous carbon nanosheet arrays (NCNA). NCNA vertically grown on carbon cloth (CC) has improved wettability and allows for the $CeO_2$/Co heterostructure to be easily accessible. The abundant intrinsic oxygen vacancies in $CeO_2$ bring the catalyst an excellent ability to tune the oxygen concentration during the oxygen reduction reaction (ORR) and oxygen evolution reaction (OER) processes. The integrity of the electrode accelerates the transfer of electrons from the active sites to the CC current collector. Therefore, ZAB using Co/$CeO_2$–NCNA@CC as the integrated cathode exhibits an impressive electrocatalytic performance toward both ORR and OER. The ZAB with Co/$CeO_2$–NCNA@CC cathode has an open-circuit voltage of 1.47 V and supply capacity of 784.4 mA h $g_{Zn}^{-1}$ even after 380 h operation at 5.0 mA $cm^{-2}$, which surpasses the catalysts of commercial Pt/C + $RuO_2$ and the most reported catalysts.

Received 14th February 2022
Accepted 29th March 2022

DOI: 10.1039/d2ta01188c

rsc.li/materials-a



## 1 Introduction

Oxygen reduction reaction (ORR) and oxygen evolution reaction (OER) are the key processes in the energy storage and transfer systems highly related to the oxygen reactions including fuel cells, metal–air rechargeable batteries and water electrolyzers.[1–6] However, the sluggish nature of ORR and OER in kinetics becomes one of the bottleneck problems to develop these systems.[7–9] Therefore, catalysts with high activity and good stability are required to accelerate the oxygen reaction for the applicable energy supply. The noble metals group-based catalysts such as Pt, Ru, and Ir are still the most used in oxygen reactions due to their high activity,[10–12] but commercial applications are seriously limited by their scarcity, high cost, and poor durability. Although, non-precious metal-based catalysts are given great expectations to substitute the precious metals catalysts due to the advantages of low cost,[13–16] the challenge of how to explore the non-precious catalysts with comparable activity to the precious metal catalyst and possess good durability still remains to be solved.

As a renewable energy conversion system, rechargeable zinc–air battery (ZAB) has high theoretical energy density, environmental friendliness, cost-effectiveness and intrinsic safety, and is thus receiving tremendous interest.[17–20] Since the air cathode of ZAB must afford both ORR and OER and must have the ability to make these two reactions work cooperatively during charge and discharge, it brings the catalysts more challenges. To put ZAB forward in practical technology, air cathode with high-efficient ORR/OER and good durability are highly expected. In addition to the essence of bi-functional properties,[21–23] whether they are

[a]School of Chemical Engineering, University of Science and Technology Liaoning, Anshan 114051, China. E-mail: hzhang0807@163.com; lxli2005@126.com; bgan@ustl.edu.cn

[b]Key Laboratory of Energy Materials and Electrochemistry Research Liaoning Province, Anshan 114051, China

† Electronic supplementary information (ESI) available. See https://doi.org/10.1039/d2ta01188c

noble metal or non-precious metal/oxide, the intrinsic activity of catalysts, is derived from their electronic and crystal structure,[24,25] which are highly related to dynamics of ORR/OER including adsorption, electron transfer, and intermediates formation.[26–28] To fully utilize the intrinsic activity of catalysts, there are several critically important factors. Firstly, active sites are uniformly distributed on the supports and are easier to access, facilitating greater transport of ions and molecules. Secondly, it is needed to keep the strong interaction of the catalyst particles with the support to avoid agglomeration and maintain good conductivity of the support for fast electrons transfer kinetics. More importantly, for practical applications, is the able ability to integrate the electrocatalytic materials' microstructure with the macroscopic features of the electrode to make the oxygen reaction cathode work cooperatively and synergistically.

Metal–organic frameworks (MOF) are promising precursors and templates to prepare the metal (compounds) loading carbon-supported catalysts since their emerging advantages of highly porous and containing uniformly distributed coordination metal sites.[29–32] A variety of metals and their oxides containing the intrinsic catalysis on ORR/OER such as Fe, Co, Ni has been used to prepare the MOF-derived carbon supported catalysts.[33–37] Owing to the porous carbon structure and the well-distributed active sites, MOF-derived catalysts exhibited good electrocatalytic performance on oxygen reactions.[38–40] However, because the mechanical and thermal stabilities of MOF are not strong enough, it is not easy to convert MOF into porous carbon with the completely same structure as MOF using simple carbonization processes. In addition, carbon particles prepared by the carbonization of MOF may agglomerate. These problems will hinder the widespread utilization of MOF. Therefore, the critical factors to obtaining metal-loaded porous carbon-derived MOF with good quality boils down to how well the morphology and structure of MOF-derived carbons are maintained, and the agglomeration of carbon particles is avoided.

Co and its compounds have been widely studied as catalysts in the oxygen reduction reaction because of their activity derived the unpaired electrons of 3d orbit and adjustable surface electronic structure.[9] Coincidently, Co is commonly used as the coordination element in MOF.[41] Therefore, Co-loaded MOF-derived carbons are attracting wide interest in developing the ORR/OER catalysts.[42–44] However, Co species alone are not enough to provide a comparable activity with precious metal catalysts, synthesis of heterostructure catalysts to modulate electronic structure, enhance oxygen adsorption, or tune the oxygen vacancy for synergistic effects.[45] $CeO_2$ possesses abundant intrinsic oxygen vacancies based on the reversible conversion of the nonstoichiometric oxide[46] and is regarded as oxygen storage and transfer media to tune oxygen concentration during oxygen reactions. Therefore, it is promising to utilize the advantages of $CeO_2$ for the construction of heterostructure catalysts with good bifunctions.[47,48]

Herein, an integrated cathode of a rechargeable Zn–air battery, in which, the ultrafine $CeO_2$/Co heterostructure was uniformly distributed in the N-doped porous carbon nanosheet arrays (NCNA) vertically grown on carbon cloth (Co/$CeO_2$–NCNA@CC), was successfully fabricated. Co/$CeO_2$–NCNA@CC possesses the following advantages: (i) NCNA vertically grown on carbon cloth not only directly transfers electrons between the current collector and the catalyst without using any conductive and adhesive agents but also facilitates mass transport to make active sites more accessible and utilized easier. On the other hand, the agglomeration of NCNA can be completely avoided because each NCNA is vertically grown on CC. (ii) The $CeO_2$/Co heterostructure can utilize the great oxygen tunability of $CeO_2$ to enhance the catalytic efficiency of active sites of Co species and generate a synergistic effect on the oxygen reaction. (iii) As an integrated cathode of ZAB, the Co/$CeO_2$–NCNA@CC electrocatalyst enabled rechargeable ZAB with supreme electrochemical performances in terms of a low voltage gap and outstanding long-term durability (over 380 h at a current density of 5 mA $cm^{-2}$).

# 2 Experimental

## 2.1 Synthesis of Co-MOF nanosheet arrays on carbon cloth

The carbon cloth (CC, 2 × 2 $cm^2$) was first pretreated in nitric acid solution (37 wt%) for 6.0 h and washed with ethanol and acetone several times. Then, the two-dimensional (2D) Co-MOF was grown on its surface *via* a facile solution reaction. Next, 70 mL aqueous $Co(NO_3)_2 \cdot 6H_2O$ (99%, 1.52 g) was quickly added to 70 mL aqueous 2-methylimidazole ($C_4H_6N_2$, 98%, 3.26 g) with strong stirring. Afterward, the carbon cloth was quickly immersed to the above mixture solution and kept for 4 h. After washing with deionized water and drying at 60 °C for 12 h, the 2D Co-MOF was achieved.

## 2.2 Synthesis of Co–NCNA@CC porous nanosheet arrays

The Co–NCNA@CC was obtained using a facile carbonization-acid etching process. Briefly, a piece of carbon cloth containing Co-MOF arrays was thermally annealed at 700 °C under flowing $N_2$ gas for 2 h with a ramp rate of 2 °C $min^{-1}$ and then naturally cooled to room temperature. After this, it was acid-leached in 0.5 M $H_2SO_4$ at 80 °C for 12 h and then washed with deionized water, and dried at 60 °C for 12 h. The final product was assigned to be Co–NCNA@CC. Similarly, Co-embedded nitrogen-doped carbon (Co–NC) was synthesized by the same pyrolysis process without using carbon cloth as a substrate.

## 2.3 Synthesis of Co/$CeO_2$–NCNA@CC porous nanosheet arrays

The as-synthesized Co–NCNA@CC was immersed in 100 mL of deionized water. Subsequently, 10 mg of $Ce(NO_3)_4$ was added to the above solution and stirred for 5 h. The mixture was heated to 95 °C, and then 4 mL of 6-aminocaproic acid aqueous solution (125 mg $mL^{-1}$) and 40 μL of concentrated HCl (37 wt%) were introduced successively. After reaction at 95 °C for 5 h, the sample was taken out and washed with ethanol and water, repeatedly, and dried at 60 °C (denoted as Co/$CeO_2$–NCNA@CC) for 12 h. Similarly, $CeO_2$/Co heterostructure on nitrogen-doped carbon (Co/$CeO_2$–NC) was synthesized by the same hydrolyzation process without carbon cloth as the substrate.

 

### 2.4 Preparation of Pt/C or $RuO_2$ electrode

Commercial Pt/C (20 wt%, Alfa Aesar) or $RuO_2$ was well-dispersed in diluted Nafion alcohol solution (500 μL of ethanol and 50 μL of Nafion) to form a homogeneous suspension. Then, the suspension was dropwise added onto CC with the same mass loading as that of the Co/$CeO_2$–NCNA and dried at room temperature before the test.

### 2.5 Material characterization

The structure, morphology, and compositions of the samples were characterized by scanning electron microscopy (SEM, Thermo Fisher Scientific Apreos), transmission electron microscopy (TEM, Tecnai G2 F30 S-TWIN), X-ray photoelectron spectroscopy (XPS, Kratos AXIS-SUPRA), X-ray diffraction (XRD, D8 ADVANCE), elemental analysis (GENESIS XM), temperature-programmed desorption of $O_2$ ($O_2$-TPD, Auto Chem II 2920), and contact angle tester (Dataphysics OCA50).

### 2.6 Electrochemical measurement

All of the electrochemical measurements were conducted on a rotating disk electrode (RDE) controller connected to an electrochemical workstation. To investigate the ORR activity, the catalytic activities of the air cathodes were tested at room temperature using a standard three-electrode system in 0.1 M potassium hydroxide (KOH) electrolyte (pH = 13) in an $O_2$-saturated environment, with Ag/AgCl electrode as the reference electrode, a platinum wire as the counter electrode, and a catalyst-modified glassy carbon electrode (GCE) as the working electrode. Acrylic tape (3M VHB tape) was used to secure the samples (such as Co/$CeO_2$–NCNA@CC and Pt/C on carbon cloth, 5 × 5 $mm^2$) on the glassy carbon rotating disc electrode tip (5 mm diameter). The electrochemical activity of the catalyst was investigated *via* linear sweeping voltammetry (LSV) in an $O_2$-saturated 0.1 M KOH solution with sweeping rates of 5 mV $s^{-1}$ at different rotating speeds (400–2500 rpm). Cyclic voltammetry (CV) was carried out in $N_2$/$O_2$-saturated 0.1 M KOH solution at a scan rate of 20 mV $s^{-1}$. All potentials in this study were converted to the reversible hydrogen electrode (RHE). The RHE was determined by calibrating the Ag/AgCl reference electrode in hydrogen-saturated electrolyte and thermodynamic potential was determined *via* the cyclic voltammetry scan. $E_{RHE} = E_{Ag/AgCl} + 0.209\ V + 0.059\ V \times pH$. Tafel plots were constructed using the Tafel equation, $\eta = b \log \eta j + a$, where $j$ is the current density, $b$ is the Tafel slope, and $a$ is the intercept relative to the exchange current density.

To study the ORR kinetic properties, the Koutecky–Levich equation can be used for determining the electron transfer number ($n$) for each $O_2$ molecule at different rotation rates:

$$\frac{1}{J} = \frac{1}{J_k} + \frac{1}{J_L} = \frac{1}{J_k} + \frac{1}{B\omega^{1/2}} \quad (1)$$

$$B = 0.62nFC_0D_0^{2/3}\nu^{-1/6} \quad (2)$$

$$J_k = nFkC_0 \quad (3)$$

where $J$, $J_k$ and $J_L$ are the measured current density, kinetic and diffusion-limiting current densities, respectively. $\omega$ is the angular velocity of the disk ($\omega = 2\omega N$, $N$ is the rotation speed), $n$ is the electron transfer number, $F$ is the Faraday constant ($F$ = 96 485 C $mol^{-1}$). In 0.1 M KOH electrolyte, the values of diffusion coefficient and saturation concentration of $O_2$ are 1.9 × $10^{-5}$ $cm^2$ $s^{-1}$ ($D_0$) and 1.2 × $10^{-6}$ mol $cm^{-3}$ ($C_0$), respectively. The kinematic viscosity ($\nu$) of the electrolyte was 0.01 $cm^2$ $s^{-1}$ and $k$ is the electron transfer rate constant. The number of electrons "$n$" was obtained by calculating the slope of $J^{-1}$ *vs.* $\omega^{-1/2}$ in the plot. Rotating ring electrode (RDE) tests were conducted at a rotation speed of 1600 rpm with a scan rate of 10 mV $s^{-1}$ in $O_2$-saturated 0.1 M KOH solution.

The polarization curves for OER were measured at the scan rate of 5 mV $s^{-1}$ in 1.0 M KOH. The electrochemical surface area (ECSA) was calculated from the electrical double layer capacitance ($C_{dl}$) measurements, which were cycled at scan rates of 5, 10, 15, 20, 25 and 30 mV $s^{-1}$ with a potential range from 0.95 to 1.02 V *vs.* RHE.

### 2.7 Zn–air battery test

The air electrode was prepared by rolling the catalyst, which was loaded on carbon cloth onto a gas diffusion layer and nickel foam to form an air electrode. Nickel foam was used as the current collector for the air cathode. In order to ensure reversible zinc electrochemical reactions at the Zn anode, a rechargeable zinc–air battery was assembled using the as-prepared air-cathode, polished zinc plate as the anode, and 6 M KOH aqueous solution with 0.2 M $Zn(CH_3COO)_2$ as the electrolyte. The air cathode had an effective contact area of 1 $cm^2$ to the electrolyte and air. Measurements were carried out at 25 °C with an electrochemical workstation (CHI 660E). The polarization curve measurements were performed using LSV at 5 mV $s^{-1}$ and power density plots were obtained using a galvanodynamic method. The galvanodynamic charge and discharge profiles of the battery were obtained by scaling the current density from 2 to 50 mA $cm^{-2}$. A cycling test was performed using the recurrent galvanostatic pulse method with 15 min discharges with a constant current density of 5 mA $cm^{-2}$. Both the current density and power density were normalized to the effective surface area of the air electrode. The specific capacity was calculated from the galvanostatic discharge curve, normalized to the mass of consumed Zn anode.

## 3 Results and discussion

### 3.1 Structural and surface chemistry of catalyst

The fabrication process of the integrated cathode of Co/$CeO_2$–NCNA@CC and the corresponding morphology and structure of samples are shown in Fig. 1. Firstly, carbon cloth was simply treated in an $HNO_3$ solution by a hydrothermal method to improve the surface activity of CC for MOF growth, which did not alter the pristine morphology of CC as shown in Fig. 1b. Then, CC was immersed in a certain amount of 2-methylimidazole (2-MeIm) solution containing $Co^{2+}$ at room temperature for 4.0 h to obtain the material of Co-MOF nanosheet

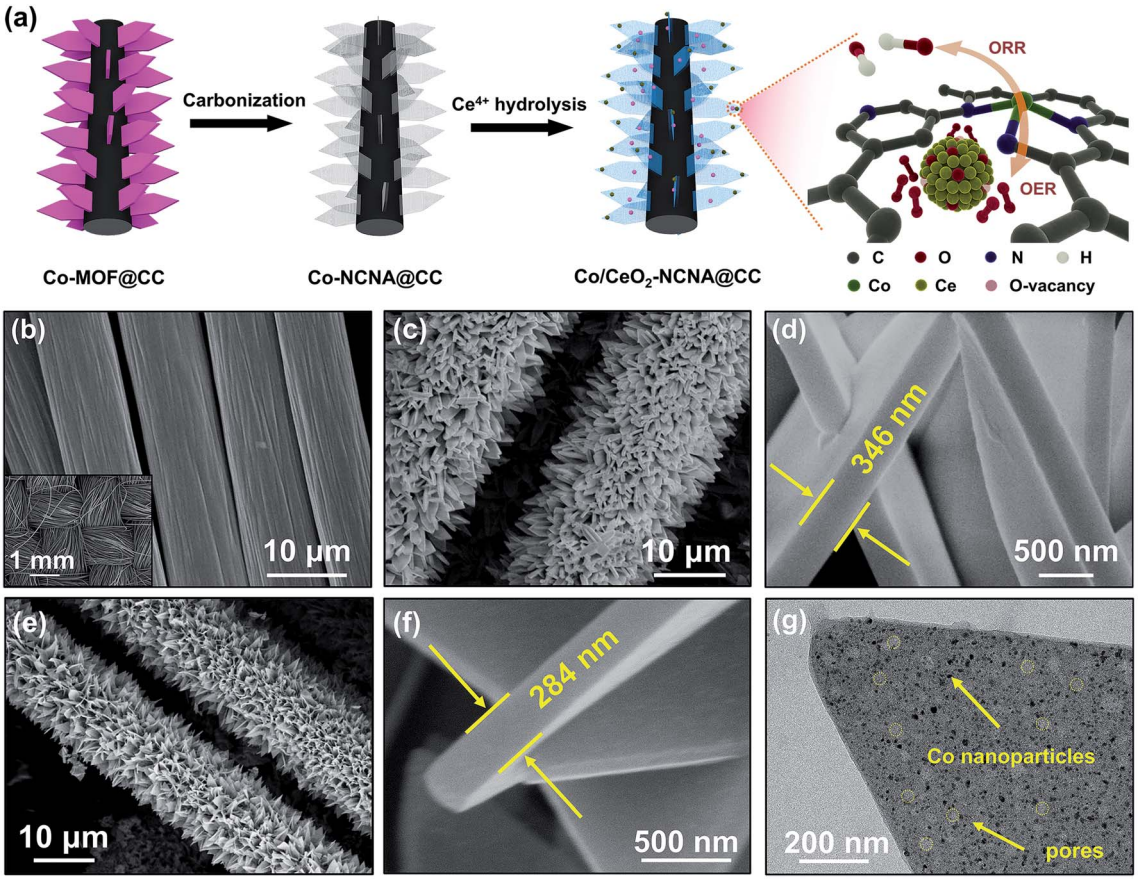


Fig. 1 (a) Schematic illustration of the fabrication of the integrated cathode of Co/$CeO_2$–NCNA@CC. SEM images of (b) $HNO_3$-treated carbon cloth, (c) and (d) Co-MOF@CC, (e) and (f) Co–NCNA@CC. TEM images of (g) Co–NCNA@CC.

arrays vertically grown to CC, which formed Co-MOF@CC. The scanning electron microscopy (SEM) images (Fig. 1c, d and S1a†) demonstrate that the Co-MOF nanosheet has an average thickness of about 346 nm and width of about 1.2 μm and is uniformly and vertically grown on CC. It can be noted that almost every MOF nanosheet is isolated when grown on CC to form the arrays, which could avoid the agglomeration of nanosheets in the next step of heat treatment. The structure of a single nanosheet was further examined using a transmission electron microscope (TEM) as shown in Fig. S1b;† one can see that the Co-MOF@CC nanosheets have solid features with a smooth surface. As shown in Fig. 1e and S1c,† the morphology of Co-MOF nanosheet arrays was well maintained after the carbonization and the acidic etching to remove the inactive Co species (Fig. S2†). During annealing in the $N_2$ atmosphere, the organic ligands from MOF were transformed into nitrogen-doped porous carbon and a part of the Co ions were reduced to Co nanoparticles. As a result, Co nanoparticles embedded to nitrogen-doped carbon nanosheet arrays grown on carbon cloth (Co–NCNA@CC) can be successfully obtained. The average thickness of Co–NCNA@CC shrinks to about 284 nm (Fig. 1d and f) from the original Co-MOF nanosheets (346 nm). As shown in Fig. 1g and S3,† the porous structure, and plenty of tiny Co nanoparticles with average diameters of 13 nm uniformly distributed in the carbon matrix can be observed. Such a porous structure can not only improve the accessibility of active sites but also facilitate the fast dissipation of gaseous products during electrocatalysis. The content of Co in the Co–NCNA@CC is 0.81 wt% (Table S1†) measured using inductively coupled plasma (ICP). The integrated cathode can be illustrated by the macroscopic appearance as shown in Fig. S4,† the full preparation process can keep the integrity of Co–NCNA@CC.

To utilize the advantages of $CeO_2$ in tuning oxygen vacancies, the heterostructure of $CeO_2$/Co was constructed through a successive hydrolysis reaction process. It can be seen that the hydrolysis reaction does not alter the morphology of the MOF-derived NCNA (Fig. 2a–c and S5†). Moreover, it can be clearly observed from the TEM images (Fig. 2d) that the ultrafine $CeO_2$ nanocrystals with sizes 5 to 8 nm were successfully obtained (Fig. 2f and S6†). The high-resolution TEM (HR-TEM) image in Fig. 2e demonstrates the lattice spacing of 0.31 nm corresponding to the (111) plane of $CeO_2$ interfaced with Co indexing by lattice spacing of 0.20 nm of the (111) plane. The elemental mapping analysis of Co/$CeO_2$–NCNA@CC reveals a uniform distribution of C, N, O, Co and Ce over the profile of the nanosheet (Fig. 2g). As shown in the X-ray diffraction (XRD) pattern of Co/$CeO_2$–NCNA@CC (Fig. 3a), the diffraction peaks at $2\theta$ values of 28.5°, 47.4°, 56.3°, 76.6° are corresponding to the (111), (220), (311) and (420) planes of the $CeO_2$ (JCPDS: 34-0394), respectively. The perspective views of the unit cells of $CeO_2$

 

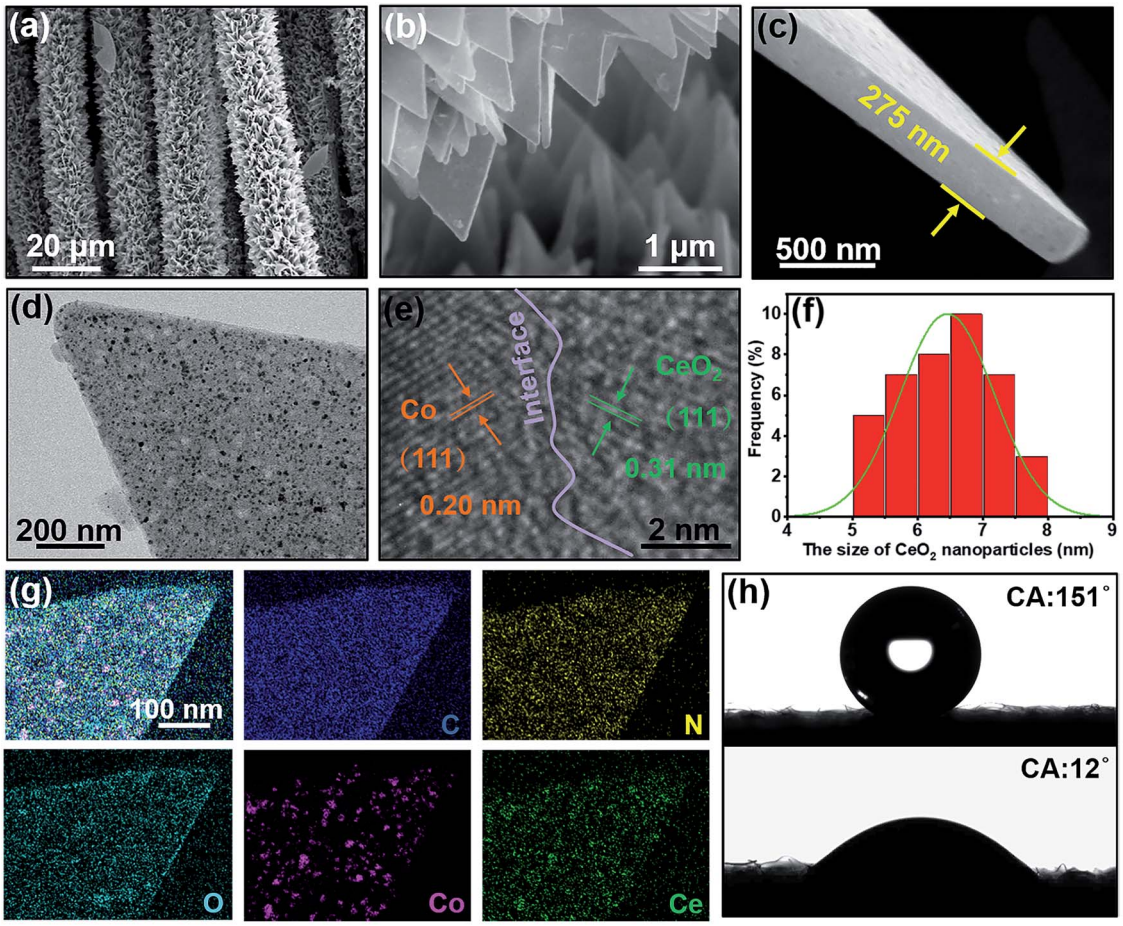


Fig. 2 (a–c) SEM images of Co/$CeO_2$–NCNA@CC. (d) TEM and (e) HRTEM images of Co/$CeO_2$–NCNA@CC. (f) Normal distribution plot of $CeO_2$ nanoparticles. (g) Elemental mapping results of mixed elements C, N, O, Co and Ce. (h) The contact angle of CC and Co/$CeO_2$–NCNA@CC.

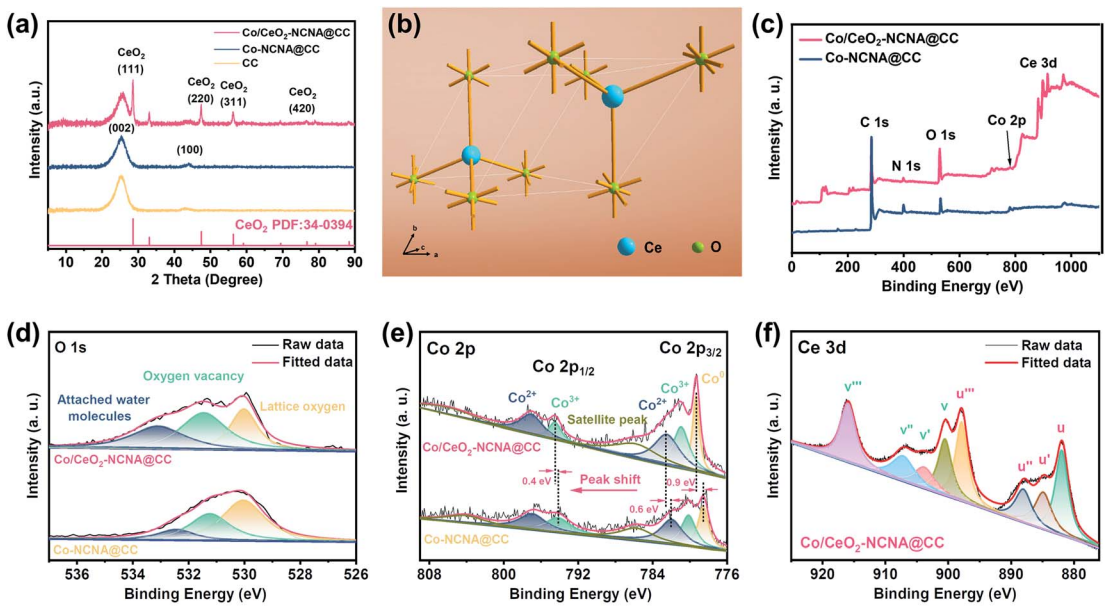


Fig. 3 (a) XRD patterns of CC, Co–NCNA@CC and Co/$CeO_2$–NCNA@CC. (b) The unit cell of $CeO_2$ structures. XPS spectra of (c) survey, (d) O 1s, (e) Co 2p, and (f) Ce 3d for Co/$CeO_2$–NCNA@CC and Co–NCNA@CC.

(space group $P6_3/mmc$ (194)) are shown in Fig. 3b, confirming that the $CeO_2$ nanocrystals have been successfully introduced into the composites, which could be promising to support a synergistic effect on oxygen reaction catalysis. The feature of porous structure and uniform multiphase distribution of Co/$CeO_2$–NCNA@CC bring improved surface hydrophilicity. As shown in Fig. 2h, carbon cloth has an obvious hydrophobicity with a contact angle of 151°, as a current collector, which may adversely impact the adsorption of reagents onto the cathode in the subsequent reaction. However, Co/$CeO_2$–NCNA grown on CC results in a sharp decrease of the contact angle to 12°. The improved wettability of the Co/$CeO_2$–NCNA@CC electrode not only enhances the interaction of reagents with the active sites but also promotes mass transport for electrocatalytic reaction kinetics.[49] Therefore, it will contribute to the electrocatalysis performance of the integrated cathode of the Zn–air battery.

The chemical state of samples is highly related to the intrinsic electrocatalysis activity. X-ray photoelectron spectroscopy (XPS) was used to investigate the surface chemical state and bonding configuration of Co–NCNA@CC and Co/$CeO_2$–NCNA@CC. XPS survey spectra of Fig. 3c confirm the surface elemental composition of C, N, O, Co in Co–NCNA@CC and the additional element of Ce in Co/$CeO_2$–NCNA@CC. The peaks corresponding to C 1s (284.6 eV), N 1s (398.0 eV), O 1s (531.5 eV) and Co 2p (780.7 eV) can be detected for both the samples. The peaks at around 886.0 eV are assigned to Ce 3d suggesting the successful introduction of Ce element in Co/$CeO_2$–NCNA@CC. These elemental contents in both samples are shown in Tables S1 and S2.†

The high-resolution spectrum of N 1s, O 1s, Co 2p and Ce 3d are shown in Fig. S7† and 3d–f. The N 1s spectra indicate four types of N containing species of pyridinic N (398.5 eV), Co–$N_x$ (399.3 eV), pyrrolic N (400.4 eV) and graphitic N (401.2 eV) in both samples, which should be produced during the conversion of Co-MOF nanosheet arrays into Co–NCNA. Apart from improving the wettability, N-containing functional groups such as pyridinic-N and graphitic-N can enhance oxygen adsorption, weak O–O band and thus have electrocatalytic activity in the basic electrolyte.[50] Furthermore, it has been identified that Co–$N_x$ sites show significant activity in the reversible oxygen reactions.[51] As shown in Fig. 3d, the high-resolution spectra of O 1s can be decoupled into three characteristic peaks located at 533.1, 531.4 and 529.9 eV, respectively, derived from the adsorbed molecular water, the surface oxygen vacancies, and the lattice oxygen arising from metal oxides.[52,53] Compared to Co–NCNA@CC, the larger peaks area percentage for the oxygen vacancies fraction in Co/$CeO_2$–NCNA@CC implies that the introduction of $CeO_2$ significantly enlarges the tuning spaces for oxygen species and the existence of more oxygen vacancies. In the Co 2p spectrum (Fig. 3e), the peaks of the binding energy at 779.9 eV and 793.9 eV correspond to the characteristics of $Co^{3+}$, while the peaks at 781.6 eV and 796.4 eV are assigned to $Co^{2+}$. Both $Co^{2+}$ and $Co^{3+}$ are attributed to Co–$N_x$ species.[54,55] Moreover, a sharp peak at 778.3 eV assigned to $Co^0$ can be clearly observed in Co/$CeO_2$–NCNA@CC, which should be produced by carbothermal reduction of Co ions during the carbonization of Co-MOF nanosheet arrays. It is especially noted that the introduction of $CeO_2$ results in the peaks Co $2p_{3/2}$ and Co $2p_{1/2}$ positively shifting to 0.6 and 0.4 eV, respectively. This phenomenon suggests a strong chemical binding of $CeO_2$/Co heterostructure, which makes Co centers more positively charged and thus facilitates the electrostatic attraction of more anionic intermediates for a fast redox process in the alkaline medium.[56] When $OH^-$ is oxidized and oxygen is released from the active site of Co species, the oxygen vacancy on $CeO_2$ can enhance $OH^-$ adsorption due to the ability to fast store oxygen in $O_2$-rich conditions.[57] Thus, the charge transfer effect may accelerate the redox process and enhance the OER performance of the catalyst. Fig. 3f depicts the Ce 3d-level spectrum that was fitted into Ce $3d_{3/2}$ (marked as V) and Ce $3d_{5/2}$ (marked as U) spin–orbit states. The peaks represented as V, V″, V‴, U, U″ and U‴ are ascribed to the characteristic peaks of $Ce^{4+}$, while the deconvoluted V′ and U′ peaks around 905.9 and 885.5 eV can be assigned to $Ce^{3+}$, which indicates the coexistence of $Ce^{3+}$ and $Ce^{4+}$ valence states in $CeO_2$.

### 3.2 Electrocatalytic activity of Co/$CeO_2$–NCNA@CC toward ORR/OER

The ORR catalytic activity of Co/$CeO_2$–NCNA@CC was firstly tested by cyclic voltammetry (CV). As shown in Fig. S8,† Co/$CeO_2$–NCNA@CC shows an obvious reduction peak centering at 0.79 V (*vs.* RHE) in the $O_2$-saturated electrolyte, which confirms the ORR activity of Co/$CeO_2$–NCNA@CC. The linear sweep voltammetry (LSV) curves of samples in Fig. 4a and S9† shows that Co/$CeO_2$–NCNA@CC possesses the most positive half-wave potential ($E_{1/2}$ = 0.77 V) and the highest limiting current of ORR, which is even better than that of the Pt/C catalyst ($E_{1/2}$ = 0.75 V, which was cast onto CC with the same mass loading amount as the Co/$CeO_2$–NCNA@CC, Fig. S10†). Koutecky–Levich (K–L) plots of Co/$CeO_2$–NCNA@CC shown in Fig. S11† suggest a high-efficiency four-electron pathway of ORR. The results demonstrate the advantages of unique nanosheet array structures vertically grown on CC making more active sites exposed, consequently, it brings better electrocatalysis. To evaluate the catalytic stability, the long-term CV and the accelerated durability test (ADT) test were carried out. As shown in Fig. 4b, Co/$CeO_2$–NCNA@CC exhibits superior long-term stability for ORR, the retention percentage of the limit current is 85.7% after 60 h operation, however, it is only 73.3% for Pt/C catalyst after 8 h of the operation. Polarization curves of Co/$CeO_2$–NCNA@CC (Fig. S12a†) show the minimal degradation of $E_{1/2}$ with only 9 mV after 50 000 cycles. As XPS spectra of O 1s are shown in Fig. S13,† the binding energy and peak area percentage of oxygen vacancies have little change after ORR long-term stability tests on Co/$CeO_2$–NCNA@CC, indicating good stability of oxygen vacancy for the ORR catalyst. The methanol tolerance was investigated by adding methanol into the electrolyte solution during the test. As shown in Fig. S12b,† the current density of Co/$CeO_2$–NCNA@CC occurs at very slight fluctuation, however, Pt/C suffers a sharp decrease mainly due to Pt oxidation by methanol.[65] Since $SCN^-$ can combine with the Co atom in Co–$N_x$ to cover up its catalytic activity,[66] KSCN solution was added to the electrolyte to investigate the influence of the introduction of Co–$N_x$ sites on the catalytic activity of Co/$CeO_2$–NCNA@CC. As shown in Fig. S14,† after adding $SCN^-$, the limit current at 0 V decreases by 17%, and its initial potential also

 

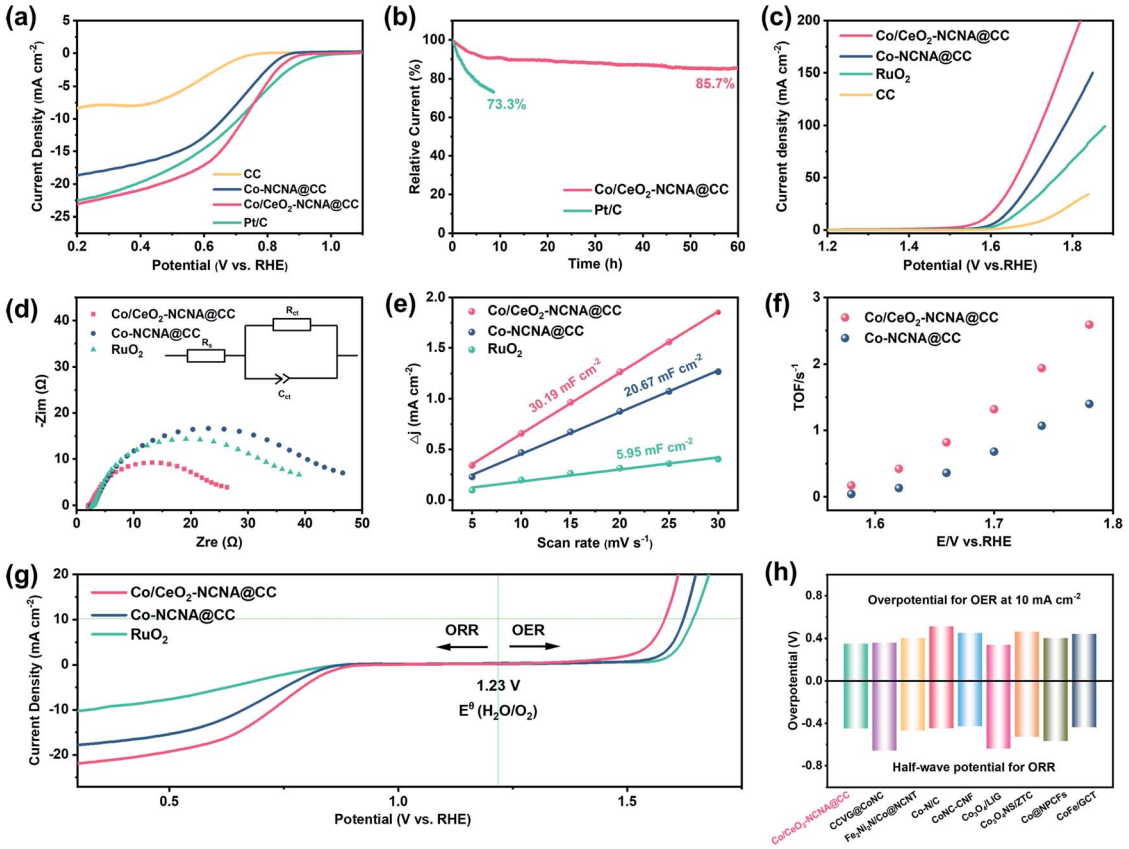


Fig. 4 (a) LSV curves of CC, Co–NCNA@CC, Co/$CeO_2$–NCNA@CC and Pt/C in 0.1 M KOH electrolyte with the rotating rate of 1600 rpm. (b) Stability tests on Co/$CeO_2$–NCNA@CC and 20% Pt/C in $O_2$-saturated 0.1 M KOH were carried out by chronoamperometry. (c) OER polarization curves, (d) electrochemical impedance spectroscopy (EIS), the inset is the fitting circuit, (e) $C_{dl}$ values, and (f) TOFs with respect to Co and Ce atoms in Co/$CeO_2$–NCNA@CC at different potentials. (g) The overall LSV curves for ORR and OER of Co/$CeO_2$–NCNA@CC, Co–NCNA@CC and $RuO_2$. (h) Comparison of the $\Delta E$ values ($\Delta E = E_{j=10} - E_{1/2}$) for Co/$CeO_2$–NCNA@CC and the recently reported bifunctional catalysts.[58–64]

decreases from 0.92 V to 0.86 V, indicating that Co–$N_x$ sites play a key role in the highly electrocatalytic activity of ORR. It can be also noted that after the introduction of $CeO_2$, the half-wave potential is 20 mV higher than that of Pt/C (Fig. 4a), which is attributed to $CeO_2$ playing an essential role as an effective catalyst for "oxygen buffer" to regulate the oxygen density of catalyst surfaces during ORR.[47] The charge imbalance of $Ce^{3+}$ ions generates oxygen vacancies and unsaturated chemical bonds in the $CeO_2$ nanocrystals and thus continually increases the oxygen absorption as well as the oxygen supplied to Co species.[67] Meanwhile, the synergistic effects between $CeO_2$ and Co species further enhance the ORR activity.

The LSV tests of OER (Fig. 4c) show that $CeO_2$ introduction results in a significantly decreased overpotential ($\eta$) to 350 mV and more negative onset potential than the other samples, indicating the synergistic effect of $CeO_2$ and Co species. The kinetics tests (Fig. S15†) demonstrate the smallest Tafel slope of 98 mV $dec^{-1}$ of Co/$CeO_2$–NCNA@CC, suggesting a faster reaction of OER. Good dynamics of Co/$CeO_2$–NCNA@CC are also confirmed by electrochemical impedance spectroscopy (EIS) tests. As shown in Fig. 4d, the semi-circle in the high-frequency range represents the charge transfer resistance ($R_{ct}$) of the reaction; Co/$CeO_2$–NCNA@CC shows a much lower $R_{ct}$ (Table S3†) than other samples, indicating its fast reaction kinetics once more. In addition to the fast dynamic characteristics, Co/$CeO_2$–NCNA@CC also exhibits outstanding durability in that the overpotential of OER increases by only 13 mV after 3000 cycles (Fig. S16†). Furthermore, the excellent OER stability of Co/$CeO_2$–NCNA@CC is revealed by the chronoamperometric (CA) test at 1.58 V, which shows only 13.3% current decay after 55 h operation (Fig. S17†). The OER/ORR reaction dynamics are highly related to the active surface where reagents can be accessed. The electrochemical active surface area (ECSA) of the samples can be evaluated by the double-layer capacitances ($C_{dl}$). Cyclic voltammetry (CVs) was used to calculate $C_{dl}$, as shown in Fig. S18.† $C_{dl}$ was determined by calculating the slope of the linearly fitted curves, the $C_{dl}$ values of Co/$CeO_2$–NCNA@CC, Co–NCNA@CC, $RuO_2$ are 30.19, 20.67, and 5.95 mF $cm^{-2}$, respectively (Fig. 4e), suggesting the largest active surface for Co/$CeO_2$–NCNA@CC. Equally important, the vertically grown NCNA with porous structure and good hydrophilicity not only facilitates the collisions between reactants and active sites and offers a highly opened pathway for mass diffusion, but also has significantly higher turnover frequency (TOF) values for Co/$CeO_2$–NCNA@CC than those of Co–NCNA@CC at different potentials (Fig. 4f). Intrinsic activity measurements by per-site

TOF provide the evidence that Co/$CeO_2$–NCNA@CC presents the highest OER activity on a per-site basis, which is consistent with the Tafel and impedance spectroscopy results.

As a bifunctional electrocatalyst, the overall catalysis of oxygen reactions is generally assessed by the voltage gaps ($\Delta E$) between the OER potential at 10 mA $cm^{-2}$ and ORR half-wave potential metrics ($\Delta E = E_{j=10} - E_{1/2}$) and the results are shown in Fig. 4g. Remarkably, the $\Delta E$ value of Co/$CeO_2$–NCNA@CC is 0.80 V, which is smaller than that of Co–NCNA@CC (0.89 V) and $RuO_2$ (1.11 V), as well as most other bifunctional catalysts recently reported (Fig. 4h), demonstrating the superior bifunctional electrocatalytic performance of Co/$CeO_2$–NCNA@CC.

### 3.3 Application as cathode of rechargeable Zn–air battery

The integrated electrode of Co/$CeO_2$–NCNA@CC serving as the air cathode of ZAB was examined by assembling the rechargeable battery as shown in Fig. 5a and S19.† As per the references, the Co–NCNA@CC electrode and the electrode loading with a mixture of Pt/C and $RuO_2$ (Fig. S20†) were also employed as air cathodes of ZAB. The open-circuit voltage of the ZAB with Co/$CeO_2$–NCNA@CC is about 1.47 V, which is very close to the ZAB of Pt/C + $RuO_2$ (1.49 V) (Fig. 5b). The discharge polarization curves and the corresponding power density curves are depicted in Fig. 5c and S21.† The ZAB driven by Co/$CeO_2$–NCNA@CC cathode exhibits a significantly higher power density of 123 mW $cm^{-2}$ at a current density of 217 mA $cm^{-2}$, compared with the ZAB driven by Pt/C + $RuO_2$ (103 mW $cm^{-2}$ at 181 mA $cm^{-2}$), Co–NCNA@CC (68 mW $cm^{-2}$ at 127 mA $cm^{-2}$) and the reported air cathodes listed in Table S4.† ZAB of Co/$CeO_2$–NCNA@CC has the specific capacity of 784.4 mA h $g_{Zn}^{-1}$ at a current density of 5 mA $cm^{-2}$ (Fig. 5d), and contributes a high energy density of about 1011 W h $kg_{Zn}^{-1}$, which surpasses the ZAB with the cathode of Pt/C + $RuO_2$ (729.1 mA h $g_{Zn}^{-1}$; 911.3 W h $kg_{Zn}^{-1}$) or CC@Co–NCNA (692.4 mA h $g_{Zn}^{-1}$; 851.6 W h $kg_{Zn}^{-1}$). The polarization curves (Fig. 5e) further display that ZAB of Co/$CeO_2$–NCNA@CC has a smaller voltage gap of charge–discharge compared to ZAB with the cathode of Co–NCNA@CC or Pt/C + $RuO_2$ at different current densities. The voltage gap at 50 mA $cm^{-2}$ is 0.86 V for the Co/$CeO_2$–NCNA@CC, is significantly lower than that for Pt/C + $RuO_2$ (1.24 V) and the Co–NCNA@CC (1.53 V). The rate capability of ZAB was assessed by examining the change of window voltage along with current and the results are shown in Fig. 5f. ZAB of Co/$CeO_2$–NCNA@CC keeps a stable window voltage, there is only a small voltage fading of 0.19 V compared with 0.36 V of Pt/C + $RuO_2$ when the current is changed from 2 to 50 mA $cm^{-2}$. The results confirm that the introduction of $CeO_2$ to construct the heterostructure of $CeO_2$/Co can bring the cathode of ZAB great capability. The cycling stability of ZAB was tested by galvanostatic charge–discharge of 30 min for each cycle at 5 mA $cm^{-2}$ (Fig. 5g). It is worth noting that ZAB with Co/$CeO_2$–NCNA@CC cathode achieves a small

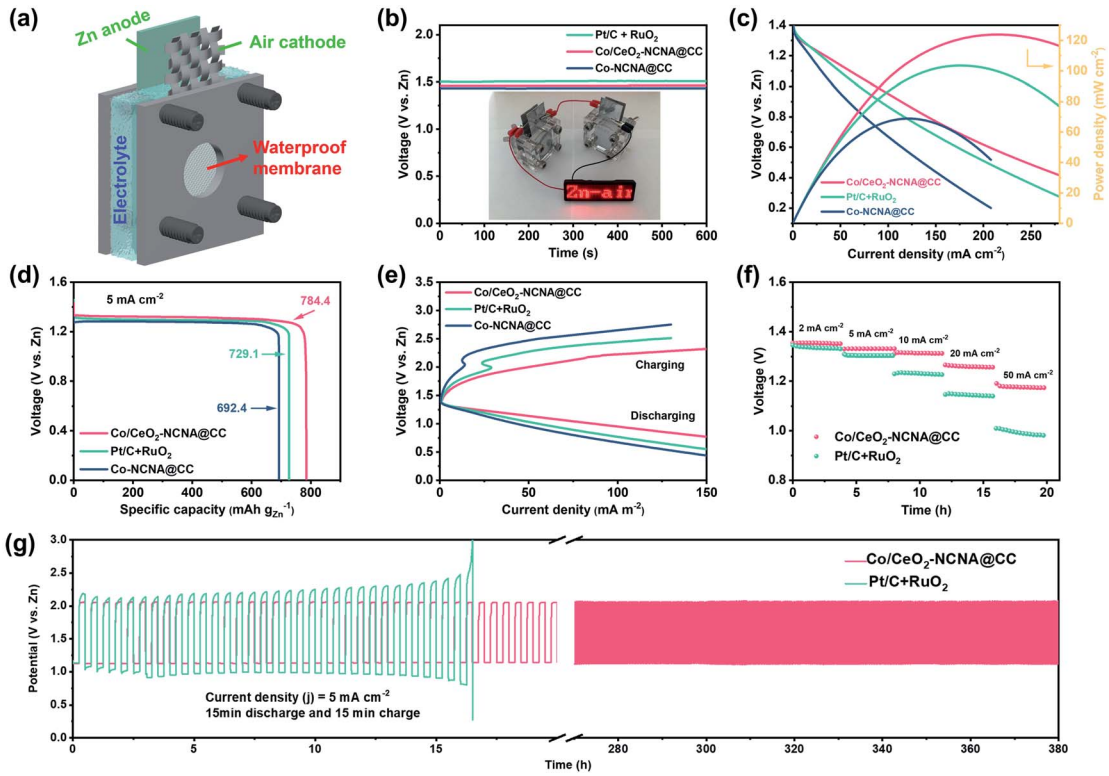


Fig. 5 (a) Schematic illustration of the zinc–air battery. (b) The open-circuit voltage, (c) discharging polarization curves and corresponding power density plots, (d) the specific capacity, and (e) discharge–charge polarization curves of the ZAB with Co/$CeO_2$–NCNA@CC, Co–NCNA@CC, and Pt/C + $RuO_2$ as the air electrode, respectively. (f) Galvanostatic discharge curves of ZAB, and (g) discharge–charge cycling curves of Co/$CeO_2$–NCNA@CC and Pt/C + $RuO_2$.

 

voltage gap of 0.96 V after the first operation of 40 h, and only a slight increase in the voltage gap after 380 h of the operation. In contrast, ZAB with the Pt/C + $RuO_2$ cathode causes a large voltage gap of 1.26 V after the operation of 16 h. The excellent stability of ZAB can be attributed to the unique integrated structure of Co/$CeO_2$–NCNA@CC. The morphology and elemental composition of Co/$CeO_2$–NCNA@CC cathode after 100 cycles (Fig. S22†) proves that the nanosheet arrays are well kept to avoid the agglomeration and elements of Co, Ce, O and N are still uniformly distributed in NCNA to supply the active sites.

### 3.4 The proposed mechanism

To characterize the $O_2$ adsorption ability and the intrinsic oxygen vacancies of catalysts, temperature-programmed desorption of $O_2$ ($O_2$-TPD) was performed for the Co embedded nitrogen-doped carbon (Co–NC) and the $CeO_2$/Co heterostructure on the nitrogen-doped carbon (Co/$CeO_2$–NC) samples and the results are shown in Fig. 6a. To eliminate the influence of the carbon cloth, Co–NC and Co/$CeO_2$–NC were prepared by a similar synthesis method without using carbon cloth as a precursor. Usually, the oxygen desorption peaks below 500 °C can be attributed to physical absorption of oxygen (~100 °C) and chemisorbed oxygen on the surface (250–350 °C).[68,69] It can be concluded according to the peak area of $O_2$-TPD that both Co–NC and Co/$CeO_2$–NC can adsorb a considerable amount of oxygen, but the latter desorbs chemisorbed oxygen at a higher temperature and intensity. It indicates that Co/$CeO_2$–NC shows a much better capability for absorbing oxygen due to the excellent ability of oxygen vacancy of $CeO_2$. Electron paramagnetic spin resonance (EPR) measurements (Fig. 6b) provide stronger evidence that $CeO_2$ has the ability to boost oxygen adsorption. Both samples show one EPR signal with a *g*-value of 2.003 that is caused by the trapped electrons due to the surface oxygen vacancies of the catalysts.[70,71] Co/$CeO_2$–NCNA@CC exhibits a stronger peak intensity, revealing its ability to contain abundant oxygen vacancies to trap more electrons. It is consistent with the $O_2$-TPD analyses and the previous XPS analysis that the introduction of $CeO_2$ alters the surface electronic structure and enhances the adsorption energy of oxygen onto the catalyst.

$$CeO_2 \leftrightarrow CeO_{2-x} + x/2O_2\ (0 \le x \le 0.5) \quad (4)$$

$$4Ce(III) + 2V_{o,s} + O_2 \rightarrow 4Ce(IV) + 2O_I^{2-} \rightarrow 4Ce(III) + 2O^* + 2V_{o,i} \quad (5)$$

On basis of the results above, a catalysis mechanism is proposed as illustrated by Fig. 6d. In the integrated cathode of Co/$CeO_2$–NCNA@CC, carbon cloth as the substrate and the current collector can enhance the electron transfer between each Co/$CeO_2$–NCNA. The porous and hydrophilic NCNA facilitate the adsorption and transport of active ions and molecules ($O_2$, $OH^-$, OOH*, O*, and $H_2O$), and enhance the effective collision between reactants and active sites. $CeO_2$ has an excellent oxygen regulation ability to boost the activity of the heterostructure of $CeO_2$/Co due to the reversible conversion between reduced and oxidized states, which can be expressed by eqn (4).[72] The catalytic mechanism involves three steps. Firstly,

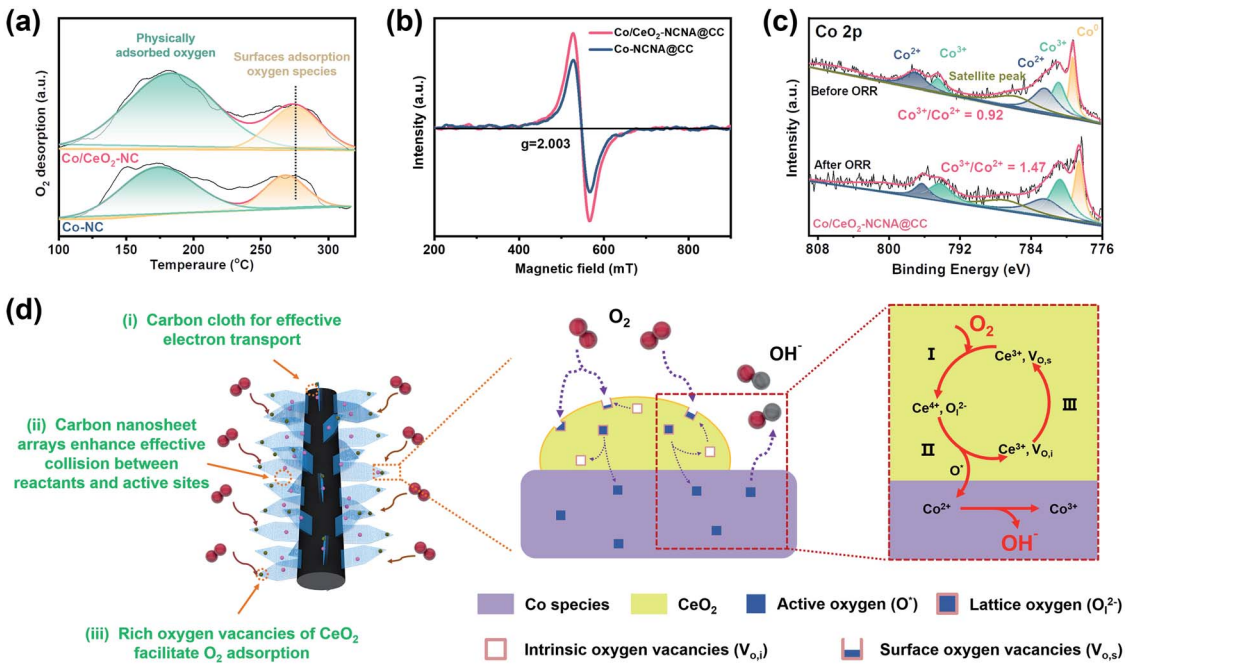


Fig. 6 (a) $O_2$-TPD profiles of Co–NC and Co/$CeO_2$–NC. (b) EPR spectra of Co–NCNA@CC and Co/$CeO_2$–NCNA@CC. (c) High-resolution XPS spectra of Co 2p for Co/$CeO_2$–NCNA@CC before and after the ORR tests. (d) Schematic diagram illustrating the structural advantages of Co/$CeO_2$–NCNA@CC in terms of electrochemical reactivity and synergistic effect.

the surface oxygen vacancies ($V_{o,s}$) in $CeO_2$ ($Ce^{3+}$) adsorb a large number of oxygen molecules to form the lattice oxygen ($O_l^{2-}$), and then $Ce^{3+}$ undergoes the oxidation to form $Ce^{4+}$ by eqn (5). Secondly, the lattice oxygen deviates its position to form active oxygen species (O*) spontaneously and leaves the intrinsic oxygen vacancies ($V_{o,i}$).[73] The O* can effectively migrate to the Co-containing active sites through the $CeO_2$/Co heterostructure and accept the electrons derived from the oxidation of $Co^{2+}$ into $Co^{3+}$. The XPS of Co/$CeO_2$–NCNA@CC before and after the ORR tests are shown in Fig. 6c. It can be noted that the percentages of $Co^{3+}/Co^{2+}$ among the Co–$N_x$ is 0.92 before the ORR test, but it increases to 1.47 after the ORR test. The significant increase in $Co^{3+}$ after the ORR test evidently suggests the mechanism that O* generates through $CeO_2$ and then traps the electrons from the oxidation of $Co^{2+}$. In the third step, the intrinsic oxygen vacancies ($V_{o,i}$) transfer to the surface of lattices, and the oxygen will fill the surface oxygen vacancies ($V_{o,s}$). The catalysis cycles illustrate that the mutual conversion of the three kinds of oxygen species promotes a continuous catalytic reaction process. The intrinsic oxygen vacancies of $CeO_2$ play as an oxygen storage station to supply oxygen species to the Co species active sites continuously, which greatly improves both half-wave potential and limiting current density.[74,75]

# 4 Conclusions

A unique integrated cathode of ZAB containing a $CeO_2$/Co heterostructure embedded in N-doped carbon nanosheet arrays (NCNA) and vertically grown onto carbon cloth (Co/$CeO_2$–NCNA@CC) has been successfully constructed by a facile carbonization-acid etching process of Co-MOF *in situ* grown on the carbon cloth and the subsequent successive hydrolysis reaction. In the integrated cathode, N-doped porous nanosheets are uniformly grown and isolated on the carbon cloth, which facilitates not only mass transport but also makes the $CeO_2$/Co heterostructure more accessible. The great oxygen tunability of $CeO_2$ enhances the catalytic activity and efficiency, and generate a synergistic effect on ORR and OER. As a result, the integrated cathode of Co/$CeO_2$–NCNA@CC exhibits outstanding bifunctional performance with $\Delta E$ of 0.80 V. In a practical application, rechargeable zinc–air batteries with the Co/$CeO_2$–NCNA@CC cathode deliver extraordinary performances with a high peak power density of 123 mW $cm^{-2}$, an ultrahigh capacity of 784.4 mA h $g_{Zn}^{-1}$ and a spectacular energy density (1011 W h $kg_{Zn}^{-1}$), which are much better than those displayed by a commercial catalyst of Pt/C + $RuO_2$.

# Conflicts of interest

There are no conflicts of interest to declare.

# Acknowledgements

The financial support from National Natural Science Foundation of China (NSFC, No. 51872131, 51972156, 51672117, 51672118, 21701077 and 22109061), Technology Liaoning Talent Project Grants (601010326) and the Distinguished Professor Project of Education Department of Liaoning are acknowledged.

# Notes and references

1 D. Wang, Y.-P. Deng, Y. Zhang, Y. Zhao, G. Zhou, L. Shui, Y. Hu, M. Shakouri, X. Wang and Z. Chen, *Energy Storage Mater.*, 2021, **41**, 427–435.
2 Y. Wang, Y.-R. Lu, C.-L. Dong and Y.-C. Lu, *ACS Energy Lett.*, 2020, **5**, 1355–1363.
3 Y. E. Song, S. Lee, M. Kim, J.-G. Na, J. Lee and J. R. Kim, *J. Power Sources*, 2020, **451**, 227816.
4 H. Huang, A. Cho, S. Kim, H. Jun, A. Lee, J. W. Han and J. Lee, *Adv. Funct. Mater.*, 2020, **30**, 2003889.
5 L.-F. Gu, J.-J. Chen, T. Zhou, X.-F. Lu and G.-R. Li, *Nanoscale*, 2020, **12**, 11201–11208.
6 Z. Liang, Q. Zou, J. Xie and Y.-C. Lu, *Energy Environ. Sci.*, 2020, **13**, 2870–2877.
7 X. F. Lu, Y. Chen, S. Wang, S. Gao and X. W. Lou, *Adv. Mater.*, 2019, **31**, 1902339.
8 J. Yan, Y. Wang, Y. Zhang, S. Xia, J. Yu and B. Ding, *Adv. Mater.*, 2021, **33**, 2007525.
9 Y. Tan, W. Zhu, Z. Zhang, W. Wu, R. Chen, S. Mu, H. Lv and N. Cheng, *Nano Energy*, 2021, **83**, 105813.
10 R. Wang, H. Yang, N. Lu, S. Lei, D. Jia, Z. Wang, Z. Liu, X. Wu, H. Zheng, S. Ali, F. Ma and S. Peng, *Chem. Eng. J.*, 2022, **433**, 134500.
11 Y. Wang, B. Liu, X. Shen, H. Arandiyan, T. Zhao, Y. Li, M. Garbrecht, Z. Su, L. Han, A. Tricoli and C. Zhao, *Adv. Energy Mater.*, 2021, **11**, 2003759.
12 M. Wu, G. Zhang, J. Qiao, N. Chen, W. Chen and S. Sun, *Nano Energy*, 2019, **61**, 86–95.
13 Z. Zhang, Y.-P. Deng, Z. Xing, D. Luo, S. Sy, Z. P. Cano, G. Liu, Y. Jiang and Z. Chen, *ACS Nano*, 2019, **13**, 7062–7072.
14 C. Mu, J. Mao, J. Guo, Q. Guo, Z. Li, W. Qin, Z. Hu, K. Davey, T. Ling and S.-Z. Qiao, *Adv. Mater.*, 2020, **32**, 1907168.
15 C. Han, W. Li, H. K. Liu, S. Dou and J. Wang, *Mater. Horiz.*, 2019, **6**, 1812–1827.
16 M. Luo, W. Sun, B. Xu, H. Pan and Y. Jiang, *Adv. Energy Mater.*, 2021, **11**, 2002762.
17 H. Wu, J. Wu, Y. Li, W. Li, J. Zhai, Q. Jiang, X. Xu and Y. Gao, *Chem. Eng. J.*, 2022, **431**, 134084.
18 Z. Xiao, C. Wu, W. Wang, L. Pan, J. Zou, L. Wang, X. Zhang and G. Li, *J. Mater. Chem. A*, 2020, **8**, 25791–25804.
19 J. Guo, L. Kang, X. Lu, S. Zhao, J. Li, P. R. Shearing, R. Wang, D. J. Brett, G. He, G. Chai and I. P. Parkin, *Energy Storage Mater.*, 2021, **35**, 530–537.
20 J. Li, Z. Meng, D. J. L. Brett, P. R. Shearing, N. T. Skipper, I. P. Parkin and S. Gadipelli, *ACS Appl. Mater. Interfaces*, 2020, **12**, 42696–42703.
21 J. Fu, R. Liang, G. Liu, A. Yu, Z. Bai, L. Yang and Z. Chen, *Adv. Mater.*, 2019, **31**, 1805230.
22 Q. Lv, W. Si, J. He, L. Sun, C. Zhang, N. Wang, Z. Yang, X. Li, X. Wang, W. Deng, Y. Long, C. Huang and Y. Li, *Nat. Commun.*, 2018, **9**, 1–11.
23 Z. Sun, Y. Wang, L. Zhang, H. Wu, Y. Jin, Y. Li, Y. Shi, T. Zhu, H. Mao, J. Liu, C. Xiao and S. Ding, *Adv. Funct. Mater.*, 2020, **30**, 1910482.

 

24 S. Zhou, X. Miao, X. Zhao, C. Ma, Y. Qiu, Z. Hu, J. Zhao, L. Shi and J. Zeng, *Nat. Commun.*, 2016, **7**, 11510.
25 M. Li, Y. Wang, G. Fu, D. Sun, Y. Li, Y. Tang and T. Ma, *Adv. Energy Mater.*, 2020, **10**, 1903833.
26 W. Cheng, X. F. Lu, D. Luan and X. W. Lou, *Angew. Chem., Int. Ed.*, 2020, **59**, 18234–18239.
27 X.-T. Wang, T. Ouyang, L. Wang, J.-H. Zhong, T. Ma and Z.-Q. Liu, *Angew. Chem., Int. Ed.*, 2019, **58**, 13291–13296.
28 J. Qian, T. Wang, Z. Zhang, Y. Liu, J. Li and D. Gao, *Nano Energy*, 2020, **74**, 104948.
29 X. F. Lu, Y. Fang, D. Luan and X. W. Lou, *Nano Lett.*, 2021, **21**, 1555–1565.
30 H. Tan, Y. Zhou, S.-Z. Qiao and H. J. Fan, *Mater. Today*, 2021, **48**, 270–284.
31 X. F. Lu, B. Y. Xia, S.-Q. Zang and X. W. Lou, *Angew. Chem., Int. Ed.*, 2020, **59**, 4634–4650.
32 Z. Liang, C. Qu, W. Guo, R. Zou and Q. Xu, *Adv. Mater.*, 2018, **30**, 1702891.
33 F. Wang, Z. Xiao, X. Liu, J. Ren, T. Xing, Z. Li, X. Li and Y. Chen, *J. Power Sources*, 2022, **521**, 230925.
34 Z. Wang, X. Ke, K. Zhou, X. Xu, Y. Jin, H. Wang and M. Sui, *J. Mater. Chem. A*, 2021, **9**, 18515–18525.
35 I. Liberman, R. Shimoni, R. Ifraemov, I. Rozenberg, C. Singh and I. Hod, *J. Am. Chem. Soc.*, 2020, **142**, 1933–1940.
36 T. Y. Ma, S. Dai, M. Jaroniec and S. Z. Qiao, *J. Am. Chem. Soc.*, 2014, **136**, 13925–13931.
37 L. Zeng, X. Cui, L. Chen, T. Ye, W. Huang, R. Ma, X. Zhang and J. Shi, *Carbon*, 2017, **114**, 347–355.
38 S. Lai, L. Xu, H. Liu, S. Chen, R. Cai, L. Zhang, W. Theis, J. Sun, D. Yang and X. Zhao, *J. Mater. Chem. A*, 2019, **7**, 21884–21891.
39 G. Li, W. Deng, L. He, J. Wu, J. Liu, T. Wu, Y. Wang and X. Wang, *ACS Appl. Mater. Interfaces*, 2021, **13**, 28324–28333.
40 Y. Liu, Z. Chen, N. Zhao, G. Tong, Z. Li, B. Wang, Y. Du, Q. Pan, Z. Li, Y. Xie and Y. Yang, *Chem. Eng. J.*, 2022, **433**, 134469.
41 J.-C. Li, Y. Meng, L. Zhang, G. Li, Z. Shi, P.-X. Hou, C. Liu, H.-M. Cheng and M. Shao, *Adv. Funct. Mater.*, 2021, **31**, 2103360.
42 N. L. Torad, M. Hu, S. Ishihara, H. Sukegawa, A. A. Belik, M. Imura, K. Ariga, Y. Sakka and Y. Yamauchi, *Small*, 2014, **10**, 2096–2107.
43 X. Yan, C.-L. Dong, Y.-C. Huang, Y. Jia, L. Zhang, S. Shen, J. Chen and X. Yao, *Small Methods*, 2019, **3**, 1800439.
44 S. Liu, Z. Wang, S. Zhou, F. Yu, M. Yu, C.-Y. Chiang, W. Zhou, J. Zhao and J. Qiu, *Adv. Mater.*, 2017, **29**, 1700874.
45 D. Yan, Y. Li, J. Huo, R. Chen, L. Dai and S. Wang, *Adv. Mater.*, 2017, **29**, 1606459.
46 C. Sun, H. Li and L. Chen, *Energy Environ. Sci.*, 2012, **5**, 8475–8505.
47 X. Li, S. You, J. Du, Y. Dai, H. Chen, Z. Cai, N. Ren and J. Zou, *J. Mater. Chem. A*, 2019, **7**, 25853–25864.
48 H. Xu, J. Cao, C. Shan, B. Wang, P. Xi, W. Liu and Y. Tang, *Angew. Chem., Int. Ed.*, 2018, **57**, 8654–8658.
49 X. Wu, J. J. Hong, W. Shin, L. Ma, T. Liu, X. Bi, Y. Yuan, Y. Qi, T. W. Surta, W. Huang, J. Neuefeind, T. Wu, P. A. Greaney, J. Lu and X. Ji, *Nat. Energy*, 2019, **4**, 123–130.
50 D. Guo, R. Shibuya, C. Akiba, S. Saji, T. Kondo and J. Nakamura, *Science*, 2016, **351**, 361–365.
51 Y. Jiang, Y.-P. Deng, R. Liang, J. Fu, R. Gao, D. Luo, Z. Bai, Y. Hu, A. Yu and Z. Chen, *Nat. Commun.*, 2020, **11**, 5858.
52 F. Arena, R. Di. Chio, L. Filiciotto, G. Trunfio, C. Espro, A. Palella, A. Patti and L. Spadaro, *Appl. Catal., B*, 2017, **218**, 803–809.
53 H. Yuan, J. Li, W. Yang, Z. Zhuang, Y. Zhao, L. He, L. Xu, X. Liao, R. Zhu and L. Mai, *ACS Appl. Mater. Interfaces*, 2018, **10**, 16410–16417.
54 H. Zhang, Z. Zhao, Y.-N. Hou, Y. Tang, J. Liang, X. Liu, Z. Zhang, X. Wang and J. Qiu, *J. Mater. Chem. A*, 2019, **7**, 9230–9240.
55 L. Zhong, Q. Huang, J. Ding, Y. Guo, X. Wang, L. Chai, T.-T. Li, Y. Hu, J. Qian and S. Huang, *J. Power Sources*, 2021, **492**, 229632.
56 M. Yu, S. Zhou, Z. Wang, J. Zhao and J. Qiu, *Nano Energy*, 2018, **44**, 181–190.
57 S. Zhang, Z.-Q. Huang, Y. Ma, W. Gao, J. Li, F. Cao, L. Li, C.-R. Chang and Y. Qu, *Nat. Commun.*, 2017, **8**, 15266.
58 Y. Zhang, H. Sun, Y. Qiu, X. Ji, T. Ma, F. Gao, Z. Ma, B. Zhang and P. Hu, *Carbon*, 2019, **144**, 370–381.
59 W. Hu, Q. Wang, S. Wu and Y. Huang, *J. Mater. Chem. A*, 2016, **4**, 16920–16927.
60 W. Zhang, X. Yao, S. Zhou, X. Li, L. Li, Z. Yu and L. Gu, *Small*, 2018, **14**, 1870109.
61 M. Ren, J. Zhang and J. M. Tour, *Carbon*, 2018, **139**, 880–887.
62 R. K. Bera, H. Park and R. Ryoo, *J. Mater. Chem. A*, 2019, **7**, 9988–9996.
63 Y. Chen, W. Zhang, Z. Zhu, L. Zhang, J. Yang, H. Chen, B. Zheng, S. Li, W. Zhang, J. Wu and F. Huo, *J. Mater. Chem. A*, 2020, **8**, 7184–7191.
64 X. Liu, L. Wang, P. Yu, C. Tian, F. Sun, J. Ma, W. Li and H. Fu, *Angew. Chem., Int. Ed.*, 2018, **57**, 16166–16170.
65 H. Chen, S. You, Y. Ma, C. Zhang, B. Jing, Z. Cai, B. Tang, N. Ren and J. Zou, *Chem. Mater.*, 2018, **30**, 6014–6025.
66 I. S. Amiinu, X. Liu, Z. Pu, W. Li, Q. Li, J. Zhang, H. Tang, H. Zhang and S. Mu, *Adv. Funct. Mater.*, 2018, **28**, 1704638.
67 J.-H. Kim, K. Shin, K. Kawashima, D. H. Youn, J. Lin, T. E. Hong, Y. Liu, B. R. Wygant, J. Wang, G. Henkelman and C. B. Mullins, *ACS Catal.*, 2018, **8**, 4257–4265.
68 W. Xia, J. Li, T. Wang, L. Song, H. Guo, H. Gong, C. Jiang, B. Gao and J. He, *ChemComm*, 2018, **54**, 1623–1626.
69 Z. Xiao, Y.-C. Huang, C.-L. Dong, C. Xie, Z. Liu, S. Du, W. Chen, D. Yan, L. Tao, Z. Shu, G. Zhang, H. Duan, Y. Wang, Y. Zou, R. Chen and S. Wang, *J. Am. Chem. Soc.*, 2020, **142**, 12087–12095.
70 L. Gui, Z. Wang, K. Zhang, B. He, Y. Liu, W. Zhou, J. Xu, Q. Wang and L. Zhao, *Appl. Catal., B*, 2020, **266**, 118656.
71 Z.-P. Wu, X. F. Lu, S.-Q. Zang and X. W. Lou, *Adv. Funct. Mater.*, 2020, **30**, 1910274.
72 K. Liu, X. Huang, H. Wang, F. Li, Y. Tang, J. Li and M. Shao, *ACS Appl. Mater. Interfaces*, 2016, **8**, 34422–34430.
73 X. Lin, S. Li, H. He, Z. Wu, J. Wu, L. Chen, D. Ye and M. Fu, *Appl. Catal., B*, 2018, **223**, 91–102.
74 M. J. Kim, G.-H. Han, S. H. Lee, H. W. Jung, J. W. Choung, C. H. Kim and K.-Y. Lee, *J. Hazard. Mater.*, 2019, **384**, 121341.
75 J. H. Lee, S. H. Lee, J. W. Choung, C. H. Kim and K.-Y. Lee, *Appl. Catal., B*, 2019, **246**, 356–366.